

Circuit QED with a graphene double quantum dot and a reflection-line resonator

Guang-Wei Deng,¹ Da Wei,¹ J.R. Johansson,² Miao-Lei Zhang,¹
 Shu-Xiao Li,¹ Hai-Ou Li,¹ Gang Cao,¹ Ming Xiao,¹ Tao Tu,¹ Guang-Can
 Guo,¹ Hong-Wen Jiang,³ Franco Nori,^{4,5} and Guo-Ping Guo^{1,*}

¹*Key Laboratory of Quantum Information,*

University of Science and Technology of China,

Chinese Academy of Sciences, Hefei 230026, China

²*iTHES research group, RIKEN, Wako-shi, Saitama, 351-0198 Japan*

³*Department of Physics and Astronomy,*

University of California at Los Angeles, California 90095, USA

⁴*CEMS, RIKEN, Wako-shi, Saitama, 351-0198 Japan*

⁵*Physics Department, The University of Michigan,*

Ann Arbor, Michigan 48109-1040, USA

(Dated: October 24, 2013)

* Corresponding author: gpguo@ustc.edu.cn

Graphene has attracted considerable attention in recent years due to its unique physical properties and potential applications. Graphene quantum dots have been proposed as quantum bits, and their excited-state relaxation rates have been studied experimentally. However, their dephasing rates remain unexplored. In addition, it is still not clear how to implement long-range interaction among qubits for future scalable graphene quantum computing architectures. Here we report a circuit quantum electrodynamics (cQED) experiment using a graphene double quantum dot (DQD) charge qubit and a superconducting reflection-line resonator (RLR). The demonstration of this capacitive coupling between a graphene qubit and a resonator provides a possible approach for mediating interactions between spatially-separated graphene qubits. Furthermore, taking advantage of sensitive microwave readout measurements using the resonator, we measure the charge-state dephasing rates in our hybrid graphene nanostructure, which is found to be of the order of GHz. A spectral analysis method is also developed to simultaneously extract: the DQD-resonator coupling strength, the tunneling rate between the DQD charge states, and the charge-state dephasing rate. Our results show that this graphene cQED architecture can be a compelling platform for both graphene physics research and potential applications.

I. INTRODUCTION

Circuit QED provides a platform for studying microwave photons and artificial atoms in electrical circuits [1, 2]. Fundamental physical phenomena and quantum algorithms have been demonstrated using spatially-separated Josephson-junction qubits coupled via superconducting microwave resonators [1, 2]. Extending this idea, theoretical works [3–10] on hybrid systems using superconducting transmission-line resonators (TLRs) and semiconducting artificial atoms have been made and there have been experiments on qubits based on carbon nanotubes [11–13], GaAs/AlGaAs [14–16], and InAs nanowires [17]. Recently, graphene has attracted considerable attention for its particular properties and variety of applications [18–20]. Due to its gapless electronic band structure and the Klein tunneling phenomena [21, 22], most graphene quantum dots are formed by the shape-effect of

etched nanostructures. This etching procedure introduces new physics related to edge states and further increases the difficulties in fabricating and manipulating the graphene nanostructures. With advanced device designs, researchers have recently realized pulsed-gate transient spectroscopy and a relaxation time of 100 ns has been measured [23] in a graphene quantum dot device. However, the dephasing times, which may be significantly shorter than the relaxation times, remain unexplored. Furthermore, there are no proposals on how to couple multiple graphene qubits of etched quantum dots.

Here we report a circuit-QED experiment with a hybrid device using a graphene etched DQD and a superconductor reflection-line resonator [24]. This provides a platform for investigating the physics of graphene nanostructures interacting with microwave photons and for exploring potential applications. A DQD-resonator coupling strength of the order of tens of MHz is demonstrated in this hybrid architecture, which is consistent with coupling strengths reported in cQED experiments using GaAs [14, 15] and InAs [17] quantum dots. In addition, this DQD-resonator architecture provides access to a sensitive dispersive microwave readout [25] mechanism for the graphene nanostructures. Previously, graphene quantum dots have only been studied using direct current (DC) transport measurements [26] or quantum-point contacts for charge sensing [27, 28]. Using a dispersive readout via the resonator, we can simultaneously extract the tunneling rate between graphene DQD charge states, the DQD-resonator coupling strength, and the dephasing rate, by measuring the resonators phase response as a function of the DQD bias at multiple probe frequencies. We find that the charge-state dephasing rates in our graphene DQD varies between 0.5 GHz and 2 GHz for different charge states.

II. THE DEVICE

Our hybrid graphene-DQD/superconducting resonator device is shown in Fig. 1. The coupling of cavity to randomly located graphene flakes is a technical challenge. To meet this challenge, we have designed and fabricated a half-wavelength superconducting reflection-line resonator consisting of two differential microstrip lines which does not require the ground plane that is indispensable in traditional transmission-line designs. The microwave field is mostly confined between the two strips, which at each point along the line has an electrical potential with opposite sign (180 degree phase shift). The RLR is coupled to a regular

transmission line via a 180 degree hybrid, which splits the microwave signal into two opposite phases [Fig. 1(a)]. The reflected microwave signal is measured using a network analyzer (NA). This RLR structure is a flexible design that could accommodate the coupling of multiple qubits (see supplementary materials).

We couple the RLR to the DQD by connecting the two strips at one end of the RLR to the two Ti/Au plunger gates LP and RP of the graphene quantum dot, see Fig. 1(b-c). This design of the RLR allows us to apply bias voltages through the two strips to facilitate the needed electrostatic confinement of the graphene DQD. The basic structure of the DQD along with an adjacent quantum point contact channel is defined by plasma etching of a large graphene flake. The electron numbers (M, N) in the left and right dots are well defined by the confinement potential induced by the LP and RP gates, respectively. An electric dipole moment of $d \sim 1000 ea_0$ is formed by the change in charge distribution as one trapped electron moves between the two potential wells of the DQD (see the supplementary materials). Here a_0 is the Bohr radius and e is the electron charge. The DQD couples to the microwave field generated by the superconducting resonator via this dipole moment. The sample is mounted in a dry dilution refrigerator with a base temperature of about 26 mK. The resonance frequency of the RLR is 6.23896 GHz and the quality factor is about 1600 with all the gates of the DQD grounded.

III. MEASUREMENT OF THE DQD THROUGH THE QPC

We first demonstrate a gate-defined graphene DQD with a QPC charge sensing measurement. In order to study electron tunneling between the two dots, and to form a dipole coupling to the microwave field, the tunneling barriers of the DQD must be made large. This also makes the resistance through the DQD large, which makes it difficult to detect DC transport through the DQD. We therefore use a nearby QPC as a charge sensor to probe the DQD. By recording the transconductance $dI_{\text{QPC}}/dV_{\text{LP}}$ as a function of the LP-RP gate voltages using a standard lock-in amplifier technique, we can measure the hexagon-like charge-stability diagram in a very large range of gate voltages. The result demonstrates that a graphene double quantum dot is formed in our device [see Fig 2(a)]. We also measured the full width at half maximum (FWHM) of the QPC signal across the $(M+1, N) \leftrightarrow (M, N+1)$ interdot transition line as a function of temperature, and we extracted the electron temper-

ature T_e , the gate lever arm α , and interdot tunneling rate $2t_C$ from the experimental data [29], see Fig. 2(d,e,f) and the supplementary materials.

IV. MEASUREMENT OF THE DQD THROUGH THE RESONATOR

We also probe the DQD using the RLR by applying a coherent microwave signal to the resonator and analyzing the reflected signal. We fix the probe frequency at 6.2385 GHz and record the amplitude A and phase ϕ of the reflected signal S_{11} , as a function of the DQD bias voltages V_{LP} and V_{RP} . Phase shifts $\Delta\phi$ and amplitude changes ΔA are observed at the triple points and on the interdot transition lines, where the charge states of the left and right dots are degenerate [see Fig. 2(b,c)]. On the cotunneling lines, no phase shift or amplitude change is detected because the charging energy (about 10 meV) of a single quantum dot is much larger than the RLR photon energy (26 μ eV). However, the RLR photon energy is close to the interdot transition energy, and the electron transitions between the dots can therefore be assisted by and detected through the RLR. Using the same LP-RP gate voltage biases as in our previous QPC measurements, we can again measure the charge-stability diagram using the phase shift and amplitude change [see Fig. 2(a-c)]. The phase shift and amplitude change are caused by a dispersive shift of the resonance frequency shift due to the interaction with the off-resonant DQD. Keeping the probe frequency $\omega_R/2\pi$ fixed, when $\omega_0/2\pi$ is shifted to lower frequencies, produces a change in ΔA and $\Delta\phi$ [see Fig. 3(e,f)]. In order to study the dipole coupling of this hybrid system, we record the phase and amplitude response while we sweep the DQD gate voltages across the $(M+1, N) \leftrightarrow (M, N+1)$ interdot transition line, corresponding to the DQD qubit energy bias ϵ being swept from negative to positive values. A two-level artificial atom is formed with an energy splitting of $\Omega = \sqrt{\epsilon^2 + 4t_C^2}$, where $2t_C$ is the tunneling splitting caused by the interdot coupling. The charge states hybridizes around $\epsilon = 0$ [see Fig. 3(a)]. The effective interaction strength is characterized by the AC susceptibility $\text{Re}(\chi)$ [see Fig. 3(b)]. We find experimentally that the resonator and the DQD can be successfully coupled. This is encouraging as it was not obvious previously to us that the coupling strength between this cavity and an atomic layered material can be sufficiently strong. We find that the phase and amplitude response sensitively depend on the graphene DQD parameters, and these relations are analyzed theoretically in the supplementary material. Although $2t_C$ generally can be tuned in this kind of etched

graphene structure using a middle gate [29], our setup lacks of this middle gate because the QPC is fabricated in its place, and we therefore cannot tune $2t_C$ in-situ. $2t_C$ is measured for a large region [see Fig. 2(a)] in our sample and is found to be larger than ω_0 . In previous work [14–17], single-peak and double-peak structures in the response of the phase and amplitude as a function of ϵ for different values of $2t_C$ have been demonstrated. The observed double-peak response is due to the changing sign of the dispersive shift when the qubit energy transition from larger to smaller than the cavity frequency, which can occur if $2t_C < \omega_0$ when $|\epsilon|$ is swept.

V. DEVICE PARAMETERS

The measured phase shift $\Delta\phi = -\arg(S_{11})$ depends on the resonance frequency ω_0 , the internal and external resonator dissipation rates κ_i and κ_e , the DQD-resonator coupling strength g_C , the DQD interdot tunneling rate $2t_C$, energy bias ϵ , energy relaxation rate γ_1 , and dephasing rate γ_2 . Here ω_0 , κ_i , and κ_e can be obtained by fitting the phase response as a function of probe frequency [see Fig. 4(a)] (see the supplementary materials), g_C can be calculated using a capacitance model, t_C can be extracted from measurements at varying temperature [29], and ϵ can be calibrated from the gate voltage lever arm measurements (6%) that is also obtained from the measurements when varying the temperature. Previous work on graphene quantum dots has reported γ_1 to be about 100 MHz [23]. This leaves γ_2 as the only remaining unknown parameter. As a example, near the DQD bias region $V_{LP} = 325$ mV and $V_{RP} = 268$ mV, where $g_C = 15$ MHz and $2t_C = 8$ GHz, by fitting the phase shift as a function of ϵ , we obtain the γ_2 for these charge states to be about 1.7 ± 0.1 GHz. Actually, g_C and $2t_C$ can also be extracted from this fitting. Previous work [16] has proven that using the resonator is more precise to measure the tunneling rates when they approach the resonator eigenfrequency ω_0 . $2t_C$ in our device is larger than ω_0 so that double peak in phase response is not observed. Moreover, g_C is found to be different for various DQD bias regions [13]. Depending on the setting of the two plunger gates, we get g_C ranging from 6.5 MHz to 20 MHz. It is particularly worth noting that the experimentally discovered g_C of the hybrid structures for graphene qubits is comparable to that for superconducting qubits and semiconductor qubits. Here the probe frequency is fixed at ω_0 . Later we will discuss a method to extract γ_2 more precisely with varying probe frequency.

VI. MEASUREMENTS AT MULTIPLE PROBE FREQUENCIES

From the theoretical analysis, we find that across the interdot transition line where $2t_C > \omega_0$, a double-peak response can also be observed with a suitable choice of probe frequency (see the supplementary materials). The narrower structures of the double-peak response, compared to the single-peak response, are more sensitive to a variety of device parameters, and therefore more suitable for parameter extraction. We therefore developed a method where multiple probe frequencies are applied to the RLR (Fig. 4(c)), which spans across the region where the double-peaked phase-shift response is observed, as a function of ϵ and for $2t_C > \omega_0$ (Fig 3). We would like to point out here this multiple probe frequency technique is particularly useful for our graphene DQD, and other systems, where the qubit parameters cannot be varied in a broad range. We extracted the phase error of our measurement setup from the measurement data. Based on this error, a simulation shows the extraction of γ_2 at the double-peak region is more precise than single-peak region for $2t_C > \omega_0$ (see the supplementary materials). We therefore fit the DQD parameters at double-peak region as $2t_C$ in our device is larger than ω_0 . For example, near the DQD bias region $V_{LP} = 302$ mV and $V_{RP} = 244$ mV, we obtain $g_C = 16.4 \pm 0.4$ MHz, $2t_C = 10.3 \pm 0.1$ GHz and $\gamma_2 = 1.6 \pm 0.1$ GHz. In another DQD bias regime, $V_{LP} = 283$ mV and $V_{RP} = 212$ mV, we obtain $g_C = 6.7 \pm 0.4$ MHz, $2t_C = 7.3 \pm 0.1$ GHz, and $\gamma_2 = 0.65 \pm 0.1$ GHz. Errors of the fitted results are small, as data was the measured and averaged until smooth curves were obtained. The variances we use here are obtained from the least-square fit, and are subject to the assumption that the model used correctly describes the measured data. The main error of this fitting comes from the converting from gate voltage to ϵ [29, 30], this may cause an error of about 20 percent for ϵ .

VII. DISCUSSION

In Ref. [16], the γ_2 in a GaAs DQD system was found to depend strongly on $2t_C$. Here we have measured different $2t_C$ in different charge-state regions and found that both g_C and γ_2 depend on the bias conditions, using a multiple-probe-frequency method. In the supplementary materials, we have analyzed the double peak region for the phase response as a function of ϵ , and we found that it is a sensitive region for extracting parameters. In

contrast to previous work [14, 16], where the resonant response as a function of ϵ has been used to extract parameters by varying $2t_C$, in our method we only tune the probe frequency. However, theoretically we find that tuning any of the free parameters, for example $2t_C$, g_C , γ_2 or ω , can result in a double-peaked phase response. In our experiment we tune the probe frequency ω because it is easy to control and can be tuned much more accurately than other parameters. Also, our method of measuring the phase shift at multiple probe frequencies could have an advantage since it does not induce variations in the DQD parameters due to changes in the DQD bias conditions (while, for example, tuning $2t_C$ might [14, 16]). In our hybrid DQD-resonator device, we demonstrate that g_C varies from 6.5 MHz to 20 MHz, and γ_2 from 0.5 GHz to 2 GHz, as the DQD bias conditions are changed. Since $g_C \ll \gamma_2$ in our device, we do not reach the strong coupling regime and we therefore do not observe vacuum Rabi splitting [31]. It is therefore important to analyze dephasing time of the graphene DQD. The dephasing time however cannot be easily obtained by normal means because paddles and edge states [27, 32–34] in graphene can mask-off its determination in charge transport based measurements. The resonant cavity, on the other hand, is primarily sensitive to the electrical dipole of the DQD and is affected substantially less by the electrostatic disorders. Indeed, the previously unknown γ_2 has been extracted for the first time in our experiment. Reducing γ_2 and reaching the strong coupling regime remains an important goal for future work.

In conclusion, we have designed and fabricated a superconducting reflection-line resonator, and for the first time coupled a resonator to a graphene double quantum dot. This provides a platform for studying the physics of light-matter interaction with graphene devices in the microwave regime. In the future, long-distance and scalable quantum information processing with graphene qubits may be possible using this circuit quantum electrodynamics architecture. We demonstrate a graphene-qubit/resonator coupling rate of around tens of MHz in this hybrid device. This is consistent with results obtained in previous experiments using semiconducting quantum dots and transmission-line resonators [14, 15]. By fitting the phase shift as a function of the graphene-qubit energy splitting, we have accurately extracted device parameters and dephasing rates of the hybrid nanostructure using multiple probe-frequency measurements. For the first time, we have measured the dephasing rate in a graphene double quantum dot, which was observed to range from 0.5 GHz to 2 GHz depending on the graphene-qubit bias conditions.

ACKNOWLEDGEMENTS

This work was supported by the National Fundamental Research Programme (Grant No. 2011CBA00200), and National Natural Science Foundation (Grant Nos. 11222438, 10934006, 11274294, 11074243, 11174267 and 91121014).

VIII. CONTRIBUTIONS

G.W.D., D.W., S.X.L., M.L.Z. and H.W.J. fabricated the samples and performed the measurements. J.R.J., F.N., H.O.L., G.C., T.T. and G.C.G. provided theoretical support and analysed the data. G.P.G. supervised the project. All authors contributed to the writing of this paper.

-
- [1] Z.-L. Xiang, S. Ashhab, J. Q. You, and F. Nori, *Rev. Mod. Phys.* **85**, 623 (2013).
 - [2] J. Q. You and F. Nori, *Nature* **474**, 589 (2011).
 - [3] L. Childress, A. Sørensen, and M. Lukin, *Phys. Rev. A* **69**, 042302 (2004).
 - [4] G.-P. Guo, H. Zhang, Y. Hu, T. Tu, and G.-C. Guo, *Phys. Rev. A* **78**, 020302 (2008).
 - [5] Z.-R. Lin, G.-P. Guo, T. Tu, F.-Y. Zhu, and G.-C. Guo, *Phys. Rev. Lett.* **101**, 230501 (2008).
 - [6] A. Cottet and T. Kontos, *Phys. Rev. Lett.* **105**, 160502 (2010).
 - [7] P.-Q. Jin, M. Marthaler, A. Shnirman, and G. Schön, *Phys. Rev. Lett.* **108**, 190506 (2012).
 - [8] C. Bergenfeldt and P. Samuelsson, *Phys. Rev. B* **87**, 195427 (2013).
 - [9] L. D. Contreras-Pulido, C. Emary, T. Brandes, and R. Aguado, *New J. Phys.* **15**, 095008 (2013).
 - [10] N. Lambert, C. Flindt, and F. Nori, *EPL* **103**, 17005 (2013).
 - [11] M. R. Delbecq, V. Schmitt, F. D. Parmentier, N. Roch, J. J. Viennot, G. Fève, B. Huard, C. Mora, A. Cottet, and T. Kontos, *Phys. Rev. Lett.* **107**, 256804 (2011).
 - [12] M. Delbecq, L. Bruhat, J. Viennot, S. Datta, A. Cottet, and T. Kontos, *Nat. Commun.* **4**, 1400 (2013).
 - [13] J. J. Viennot, M. R. Delbecq, M. C. Dartiailh, A. Cottet, and T. Kontos, *arXiv:1310.4363* (2013).

- [14] T. Frey, P. J. Leek, M. Beck, A. Blais, T. Ihn, K. Ensslin, and A. Wallraff, Phys. Rev. Lett. **108**, 046807 (2012).
- [15] H. Toida, T. Nakajima, and S. Komiyama, Phys. Rev. Lett. **110**, 066802 (2013).
- [16] J. Basset, D. Jarausch, A. Stockklauser, T. Frey, C. Reichl, W. Wegscheider, T. Ihn, K. Ensslin, and A. Wallraff, Phys. Rev. B **88**, 125312 (2013).
- [17] K. D. Petersson, L. W. McFaul, M. D. Schroer, M. Jung, J. M. Taylor, A. A. Houck, and J. R. Petta, Nature **490**, 380 (2012).
- [18] A. K. Geim and K. S. Novoselov, Nat. Mater. **6**, 183 (2007).
- [19] A. K. Geim, Science **324**, 1530 (2009).
- [20] G.-P. Guo, Z.-R. Lin, T. Tu, G. Cao, X.-P. Li, and G.-C. Guo, New J. Phys. **11**, 123005 (2009).
- [21] A. V. Rozhkov, G. Giavaras, Y. P. Bliokh, V. Freilikher, and F. Nori, Phys. Rep. **503**, 77 (2011).
- [22] A. H. Castro Neto, N. M. R. Peres, K. S. Novoselov, and A. K. Geim, Rev. Mod. Phys. **81**, 109 (2009).
- [23] C. Volk, C. Neumann, S. Kazarski, S. Fringes, S. Engels, F. Haupt, A. Muller, and C. Stampfer, Nat. Commun. **4**, 1753 (2013).
- [24] M.-L. Zhang, G.-W. Deng, S.-X. Li, H.-O. Li, G. Cao, T. Tu, M. Xiao, G.-C. Guo, H.-W. Jiang, I. Siddiqi, and G.-P. Guo, arXiv:1309.0178 (2013).
- [25] A. Blais, R.-S. Huang, A. Wallraff, S. M. Girvin, and R. J. Schoelkopf, Phys. Rev. A **69**, 062320 (2004).
- [26] L. A. Ponomarenko, F. Schedin, M. I. Katsnelson, R. Yang, E. W. Hill, K. S. Novoselov, and A. K. Geim, Science **320**, 356 (2008).
- [27] L.-J. Wang, G. Cao, T. Tu, H.-O. Li, C. Zhou, X.-J. Hao, Z. Su, G.-C. Guo, H.-W. Jiang, and G.-P. Guo, Appl. Phys. Lett. **97**, 262113 (2010).
- [28] J. Güttinger, C. Stampfer, S. Hellmüller, F. Molitor, T. Ihn, and K. Ensslin, Appl. Phys. Lett. **93**, 212102 (2008).
- [29] D. Wei, H.-O. Li, G. Cao, G. Luo, Z.-X. Zheng, T. Tu, M. Xiao, G.-C. Guo, H.-W. Jiang, and G.-P. Guo, arXiv:1307.5663 (2013).
- [30] L. DiCarlo, H. Lynch, A. Johnson, L. Childress, K. Crockett, C. Marcus, M. Hanson, and A. Gossard, Phys. Rev. Lett. **92**, 226801 (2004).

- [31] A. Wallraff, D. I. Schuster, A. Blais, L. Frunzio, R. S. Huang, J. Majer, S. Kumar, S. M. Girvin, and R. J. Schoelkopf, *Nature* **431**, 162 (2004).
- [32] F. Molitor, C. Stampfer, J. Güttinger, A. Jacobsen, T. Ihn, and K. Ensslin, *Semicond. Sci. Technol.* **25**, 034002 (2010).
- [33] M. Evaldsson, I. V. Zozoulenko, H. Y. Xu, and T. Heinzel, *Phys. Rev. B* **78**, 161407 (2008).
- [34] P. Gallagher, K. Todd, and D. Goldhaber-Gordon, *Phys. Rev. B* **81**, 115409 (2010).

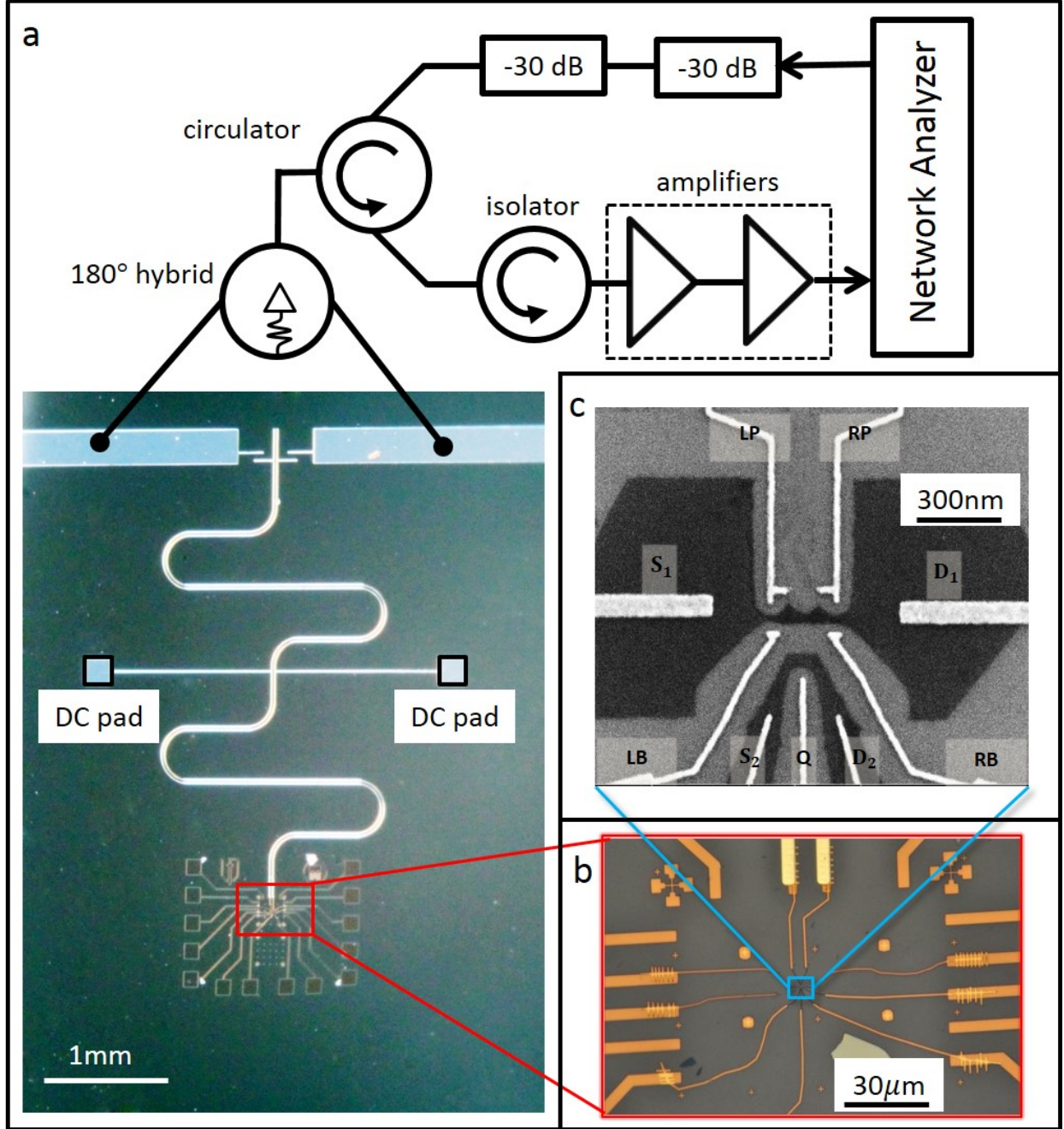


FIG. 1. **Hybrid graphene DQD/superconducting RLR device.** (a) Circuit schematic and micrograph of the hybrid device. The half-wavelength reflection-line resonator is connected to a graphene DQD at the end of its two striplines. A microwave signal is applied to the other end of the resonator, and the reflected signal is detected using a network analyzer. The DC voltage used to control the electron numbers in the DQD is applied via the two DC pads directly connected to the resonator striplines. (b) Micrograph of the DQD gate structure. (c) Scanning-electron micrograph of a typical sample of our device.

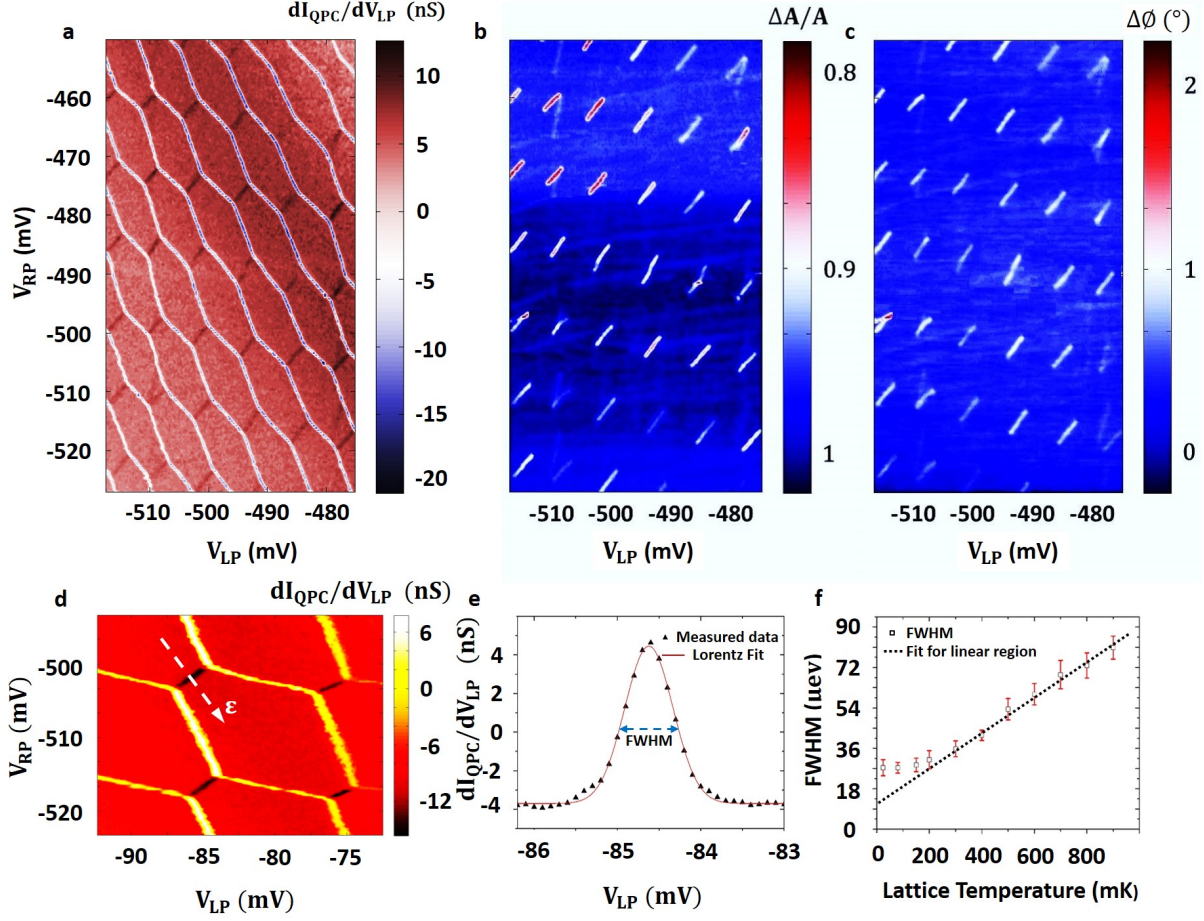


FIG. 2. Measurements of the graphene DQD charge-stability diagram. (a) The charge-stability diagram measured using a quantum-point contact. (b-c) The charge-stability diagram measured by the amplitude (b) and phase (c) response of the reflection-line resonator. The three charge-stability diagrams show a close correspondence. (d) A charge-stability diagram of a weak tunnel coupling region, used to measure the full width at half maximum (FWHM) of the QPC signal. (e) FWHM measured at the base temperature. We fit the data to a Lorentzian. (f) FWHM as a function of the lattice temperature, measured by varying the temperature of the mixing chamber. The high temperature region shows a linear dependence and $2t_C$, α , and T_e can be extracted by fitting the FWHM as a function of the lattice temperature.

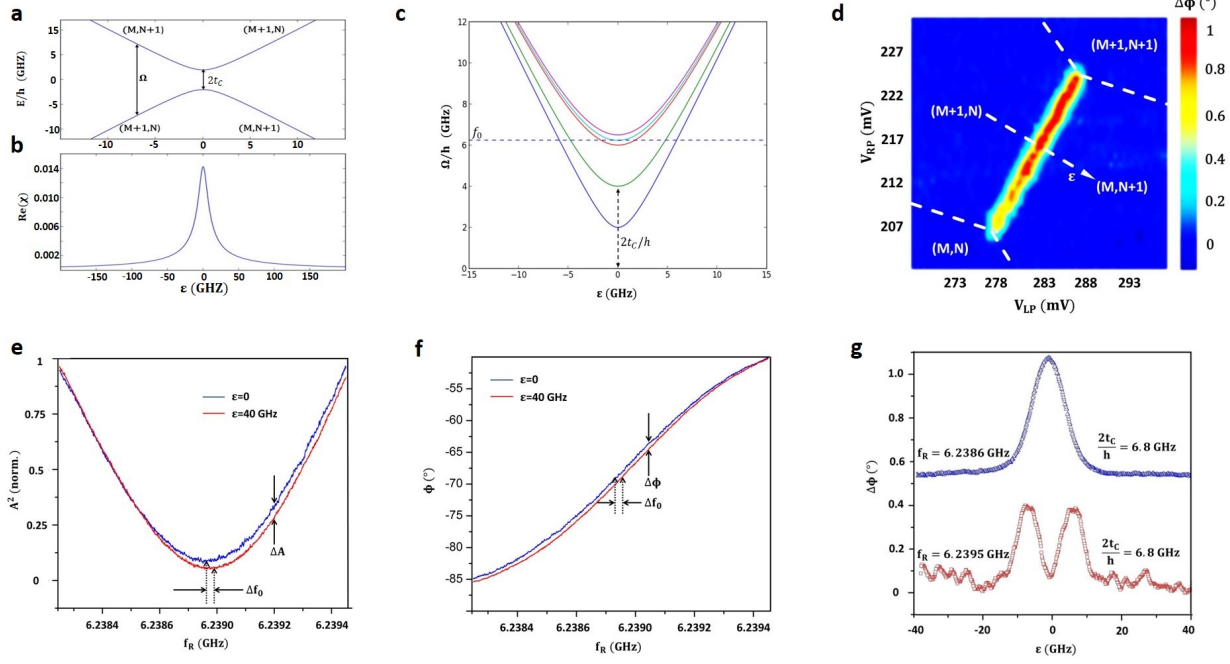


FIG. 3. **Measurements of the DQD-resonator coupling.** [note: inaccurate figure title]

(a) The DQD energy levels. (b) AC susceptibility, $\text{Re}(\chi)$, as functions of the DQD detuning ϵ . (c) The RLR resonance frequency $f_0 = \omega_0/2\pi$, compared to the DQD qubit transition frequency, Ω , for different interdot tunneling rates $2t_C$. (d) The phase response of the RLR as a function of gate voltages V_{LP} and V_{RP} near the $(M+1, N) \leftrightarrow (M, N+1)$ interdot transition line, measured at a fixed probe frequency $\omega_R/2\pi = 6.2385$ GHz. (e-f) The spectrum of the phase (e) and amplitude (f) response for $\epsilon = 0$ (blue) and for very large ϵ (red). (g) The phase response as a function of DQD detuning ϵ , in the signal-peak region (upper panel) and the double-peak region (lower panel).

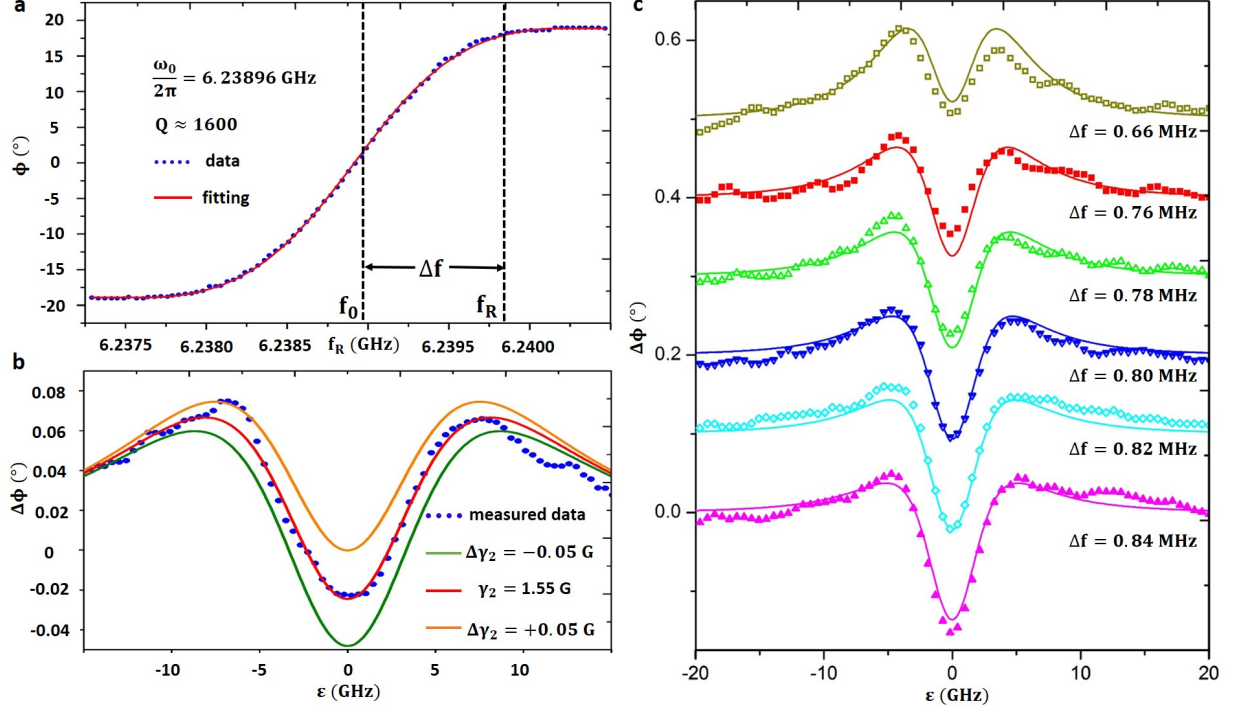


FIG. 4. **Phase response.** (a) Best-fit of the phase vs frequency curve. Quality factor and resonance center can be obtained. (b) γ_2 sensitivity to the fitting. Blue dot line is the measured data, red line shows the best-fit curve, green and yellow lines are the results with changing γ_2 at a small value $\Delta\gamma_2$. (c) Experimental data of the phase shift $\Delta\phi$, as a function of the DQD detuning ϵ , collected for the same interdot transition line as shown in Fig. 3(d). Each measurement is taken at a different probe frequency f_R , which has a detuning of the cavity $\Delta f = f_R - f_0$. The theoretical model used in the fitting is described in the supplementary materials. The free fitting parameters were $2t_C$, g_C and γ_2 , and other DQD and resonator parameters were assumed to be known from other measurements and calibrations. The extracted parameters are given in the text.

I. DEVICE AND MEASUREMENT CIRCUIT

The reflection-line resonator (RLR) consists of two coupled differential microstrip lines. A stable electromagnetic field is formed between the two microstrips when a microwave field with equal magnitude but opposite phase is applied to the resonator through the 180 degree hybrid (Fig. S1 a)[1]. The reflected signal S_{11} is measured by a network analyzer (NA). The resonator was patterned using optical lithography and a $2\ \mu\text{m}$ thick layer of photoresist. The wafer was subsequently deposited with a 200 nm thick layer of aluminum (Al), thermally evaporated at the rate of $1\ \text{\AA}/\text{s}$, and lifted-off in acetone. Aluminum is superconducting at

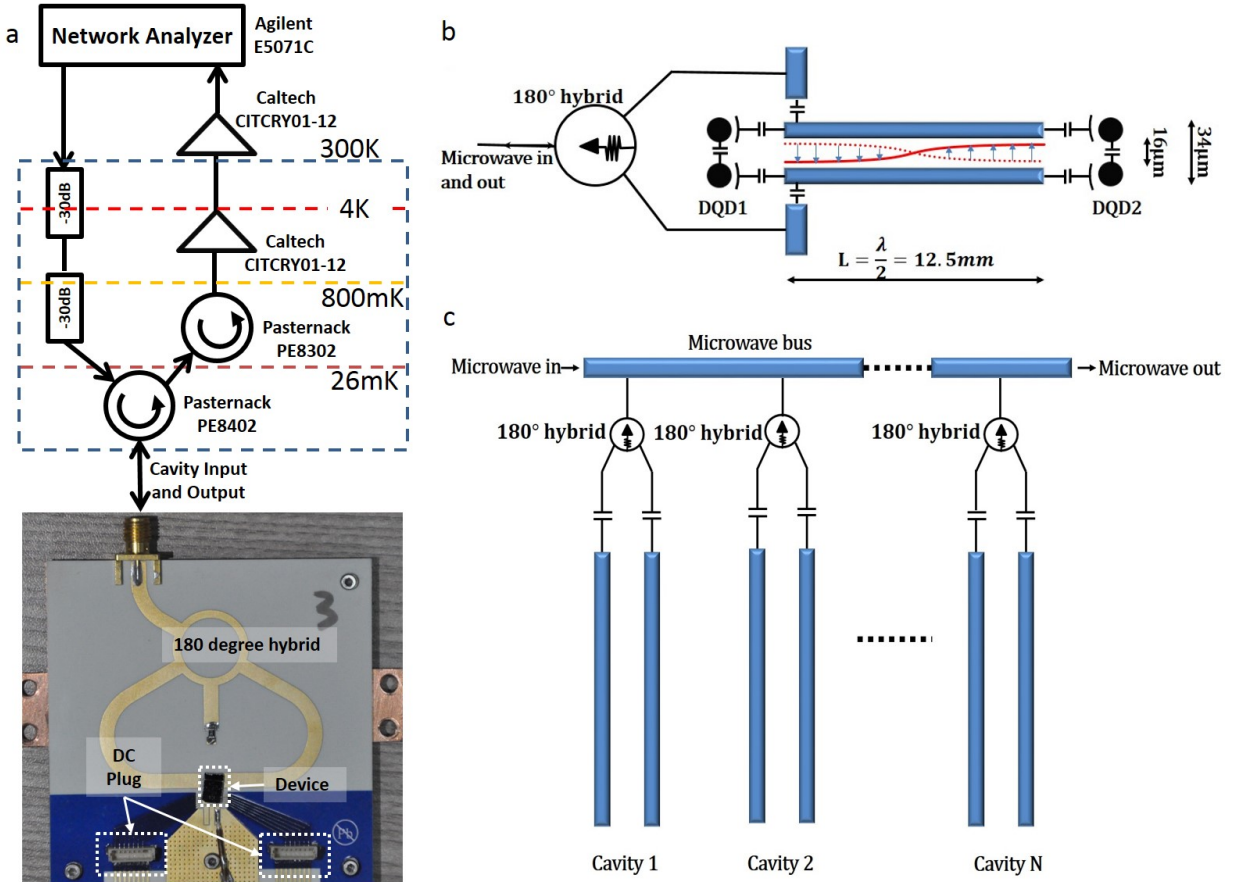


FIG. S1. Schematic diagram of the hybrid DQD/superconducting resonator device.

(a) Schematic of the measurement setup and photograph of the high-frequency sample holder. (b) Proposed design of two double quantum dot qubits coupled to a reflection-line resonator. (c) Proposed design of a scalable hybrid device with several resonators coupled to a microwave bus.

the base temperature of about 26 mK and the internal loss of the resonator can be neglected. The amplitude and phase spectra are obtained from the NA and can be fitted to the model of a $\lambda/2$ open-ended microstrip resonator [1], from which the resonance frequency and quality factor, Q , can be extracted. Most of our resonators have a resonance frequency near 6.23 GHz, and the Q factor can be varied largely from several hundred up to several tens of thousands by changing the coupling capacitance. As a resonator with large Q factor can be used as quantum storage and low Q factor is suitable for readout, we design the coupling capacitance so that the Q factor is about 5000 without coupling to the quantum dot. When the resonator is coupled to the double quantum dot, the Q factor is about 1600 for our device. This decrease of Q may be caused by current leakage through the quantum dot at the end of the resonator. The two DC gates are directly connected to the two striplines of the resonator. Computer simulations of this design, using the software HFSS, show that the DC bias and AC microwave signals do not interfere, and this has also been verified experimentally in several test samples. The input and output ports of the NA are connected to the resonator via a PE-8402 circulator and a 180 degree hybrid, which direct the signal reflected by the resonator back to the NA. Furthermore, two 30 dB attenuators are connected between the NA output port and the circulator, reducing the power applied to the resonator to -130 dBm. The reflected signal is amplified at 4 K and at room temperature, and an isolator is used to prevent noise from the amplifiers and the environment from reaching the sample.

Our device design can be extended to couple two quantum-dot qubits to one resonator; one at each end of the resonator where the antinodes of the electromagnetic field are located [Fig. S1(b)]. We can also extend the design to include multiple resonators coupled to a common microwave bus, as shown in Fig. S1(c).

II. MEASUREMENTS OF THE GRAPHENE QUANTUM DOT

Due to the small tunnelling rate from the quantum dot to the reservoirs, we were unable to measure the DC transport current through the double quantum dot. However, using a QPC we were able to perform charge-sensing measurements and obtained the charge-stability diagram of the device, shown in Fig. S2. In order to prevent the microwave power from being absorbed by the substrate, we choose undoped silicon with a 300 nm thermal

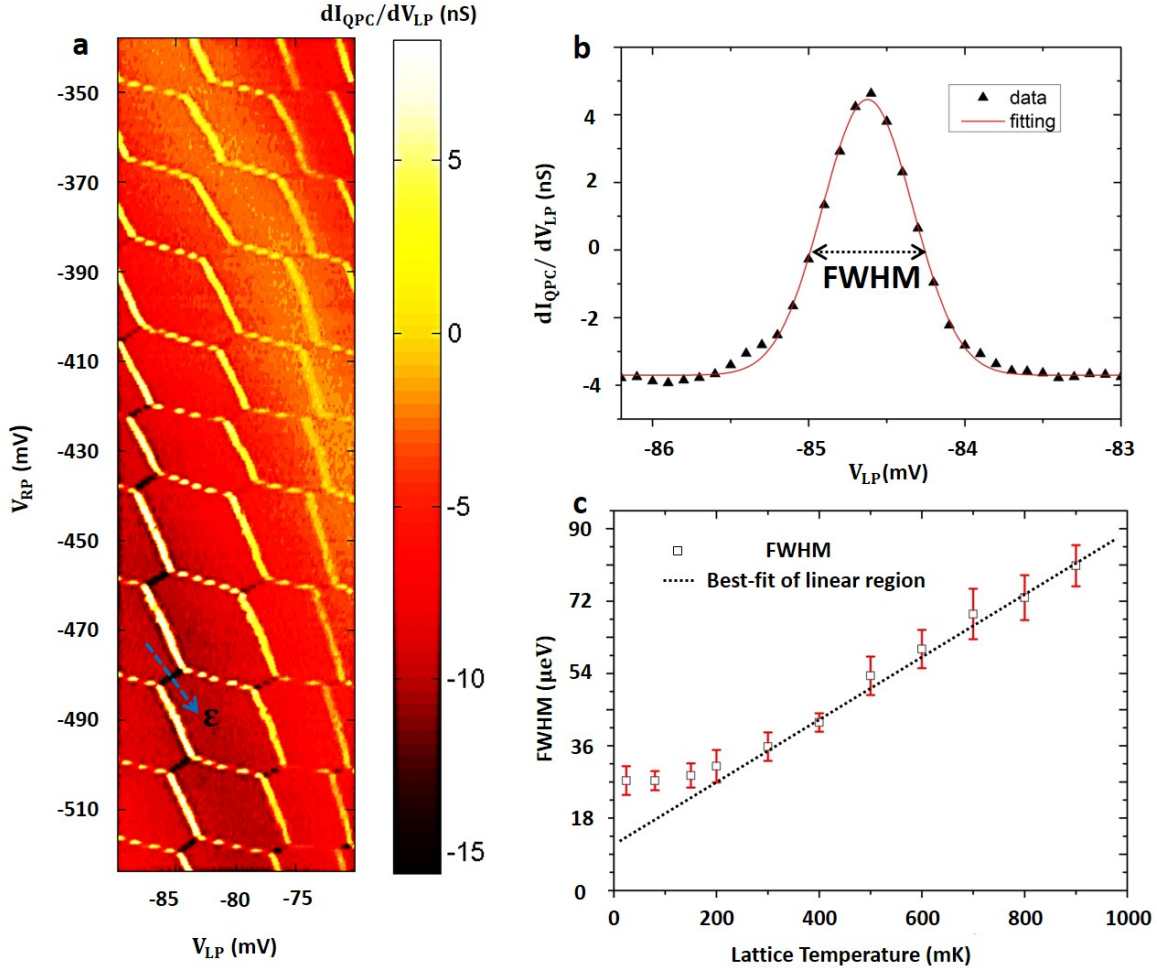


FIG. S2. **Temperature dependence measurement.** (a) The charge-stability diagram of the graphene DQD, obtained using a QPC charge-sensing measurement at the base temperature. (b) The full width at half maximum (FWHM) of the QPC signal as a function of ϵ . The FWHM is extracted from the data using a Lorentzian fit. The temperature is varied from the base temperature up to 1 K, and here we show the result at the base temperature. (c) The FWHM as a function of the lattice temperature. The dashed line is the best linear fit for the high temperature region.

oxide as substrate. The back gate is grounded during the measurement. For varying lattice temperature, we measured the full width at half maximum (FWHM) of the QPC signal as

a function of ϵ . Here $2t_C$, T_e , and the FWHM are related as [2] :

$$\frac{\tanh(\delta)}{2\delta} = \frac{\delta^2}{(\sqrt{\delta^2 + F^2})^3} \tanh(\sqrt{\delta^2 + F^2}) + \frac{F^2}{(\delta^2 + F^2)} \coth^{-2}(\sqrt{\delta^2 + F^2}), \quad (1)$$

$$F = \frac{\text{FWHM}(eV)}{2} \frac{1}{2k_B T_e}, \quad (2)$$

$$\delta = \frac{2t_C}{2k_B T_e}, \quad (3)$$

where k_B is the Boltzmann constant, T_e is the electron temperature and FWHM(eV) is the FWHM in energy unit, which can be transformed from the gate voltage by the plunger gate lever arm. Lever arm is defined as $\alpha_L = C_{LP}/C_L$, where C_L is the total capacitance of the left dot (the definition of the capacitance can be seen in Fig. S3), and the same with α_R .

By fitting the FWHM as a function of temperature, we extract $2t_C$, T_e , and the lever arm α of the plunger gates. Here different values of $2t_C$ can be obtained at different interdot charge transition states as it cannot be tuned in-situ, T_e is about 150 mK in our device, and the lever arm is about 6%.

III. CAPACITANCE MODEL FOR THE HYBRID SYSTEM

The coupling between the graphene double quantum dot and the RLR can be described by an equivalent circuit, shown in Fig. S3(a). We define

$$\nu = \frac{V_L - V_R}{+V - (-V)} = \frac{V_L - V_R}{2V}, \quad (4)$$

where ν can be understood as the lever arm between microwave energy in RLR and the graphene DQD. The coupling strength is then given by $g_C = \omega_0 \nu \sqrt{\frac{2Z_0}{R_Q}}$ [3], where $R_Q \approx 26 \text{ k}\Omega$ is the quantum resistance and $Z_0 = 50 \Omega$ is the characteristic impedance. By simple circuit analysis and the constant capacitance model [4], we obtain

$$\nu = \frac{\alpha_L + \alpha_R + \alpha_R \frac{\Delta V_{LP}}{\Delta V_{RP}} k_1 + \alpha_L \frac{\Delta V_{RP}}{\Delta V_{LP}} \frac{1}{k_2}}{1 - \frac{k_1}{k_2}} \quad (5)$$

where α_L , α_R are the lever arm of LP and RP gates respectively. The slopes k_1 , k_2 and V_{LP} , V_{RP} are shown in Fig. S3. For the interdot transition line near the region $V_{LP} = 325 \text{ mV}$, $V_{RP} = 268 \text{ mV}$, we calculate g_C to be about 15 MHz. This coupling strength is comparable to the previously reported values for semiconducting quantum dots coupled to transmission-line resonators [5, 6]. With $\hbar g_C = Ed$, and the photon-induced electric field E , of the order

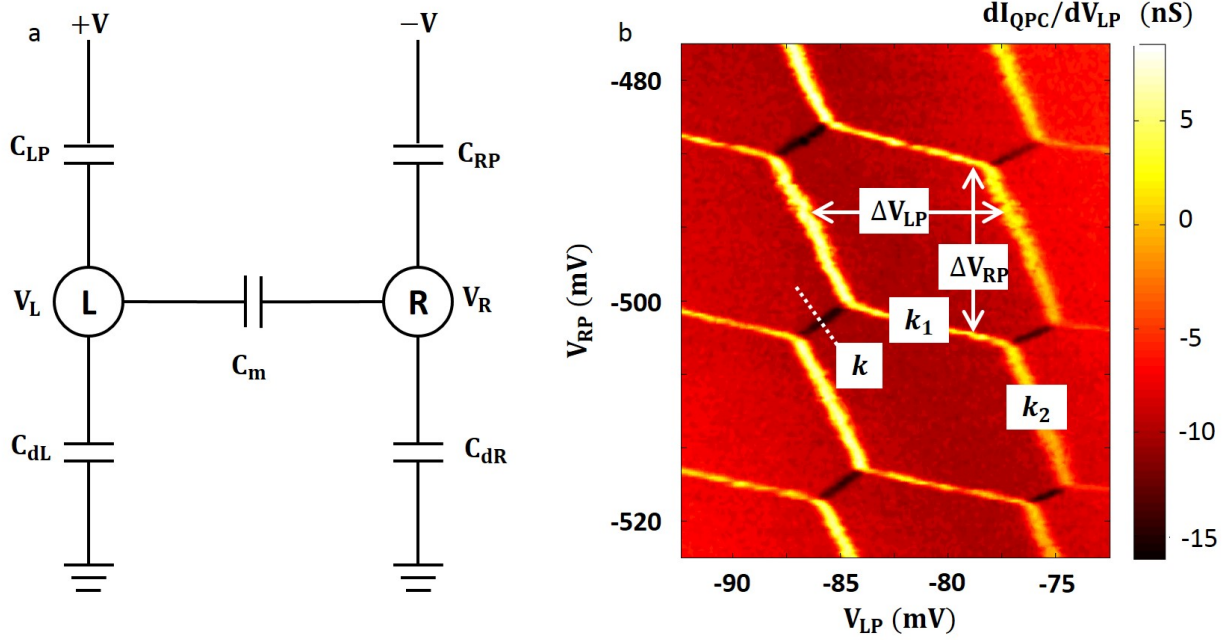


FIG. S3. **Capacitance model for the hybrid system.** (a) Equivalent circuit diagram of the hybrid system. $+V$ and $-V$ represent the equivalent voltage produced by microwave from the two pins of RLR. C_{LP} is the coupling capacitance between the LP gate and the left dot, and similarly for C_{RP} . C_m is the capacitance between the two dots. C_{dL} is the total capacitance of left dot except C_{gL} and C_m , also similarly for C_{dR} . V_L and V_R are the effective voltages induced by $+V$ and $-V$. (b) A typical charge stability diagram and definition of specify parameters.

of 10^{-1} V/m, we estimate that the dipole moment of the DQD system is of the order of $d = 1000 ea_0$, where a_0 is the Bohr radius.

IV. QUANTUM MODEL

The double quantum dot can be modeled as a quantum two-level system that couples to the resonator via a dipole interaction, described by the Hamiltonian [7]

$$H = \hbar\Delta_0 a^\dagger a + \frac{1}{2}\hbar\Delta\sigma_z + \hbar g_{\text{eff}}(\sigma_+ a + \sigma_- a^\dagger), \quad (6)$$

which is written in the qubit eigenbasis and in the rotating-frame with respect to the probe frequency ω_R and under the rotating wave approximation. Here $g_{\text{eff}} = g_C \frac{2t_C}{\Omega}$, $\Delta_0 = \omega_0 - \omega_R$, $\Delta = \Omega - \omega_R$, ω_0 is the resonance frequency of the RLR, $\Omega = \sqrt{(2t_C)^2 + \epsilon^2}$, $\Omega_\pm = \pm\Omega/2$

are the eigenenergies of the quantum dot two level system. Here σ_z is the standard Pauli z -operator, and σ_- (σ_+) and a (a^\dagger) are the annihilation (creation) operators for the quantum dot and resonator photons, respectively.

To model the internal κ_i and external κ_e dissipation of the resonator, and the qubit relaxation γ_1 and dephasing γ_2 , we first consider the Lindblad master equation on standard form

$$\dot{\rho} = -i[H, \rho] + \kappa \mathcal{D}[a]\rho + \gamma_1 \mathcal{D}[\sigma_-]\rho + \frac{1}{2}\gamma_2 \mathcal{D}[\sigma_z]\rho, \quad (7)$$

where $\mathcal{D}[a]\rho = a\rho a^\dagger - \frac{1}{2}a^\dagger a\rho - \frac{1}{2}\rho a^\dagger a$ is the Lindblad dissipator. Here $\kappa = \kappa_e + \kappa_i$ is the total dissipation rate of the resonator. The corresponding Heisenberg-Langevin equations of motion for the operators a , σ_- and σ_z are

$$\dot{a} = -i\Delta_0 a - ig_{\text{eff}}\sigma_- - \frac{1}{2}\kappa a + \sqrt{\kappa_e}a_{\text{in}}, \quad (8)$$

$$\dot{\sigma}_- = -i\Delta\sigma_- + ig_{\text{eff}}a\sigma_z - \frac{1}{2}\gamma_1\sigma_- - \gamma_2\sigma_-, \quad (9)$$

where we have neglected the quantum noise terms for the quantum dot operators. For simplicity, we will also assume that the quantum dot remains in its ground state, $\sigma_z \rightarrow -1$.

By transforming these equations to the frequency domain we obtain in the frame rotating with the driving frequency ω_R

$$\begin{aligned} -i(\omega - \omega_R)a &= -i\Delta_0 a - ig_{\text{eff}}\sigma_- - \frac{1}{2}\kappa a + \sqrt{\kappa_e}a_{\text{in}} \\ -i(\omega - \omega_R)\sigma_- &= -i\Delta\sigma_- - ig_{\text{eff}}a - \frac{1}{2}\gamma_1\sigma_- - \gamma_2\sigma_- \end{aligned} \quad (10)$$

where ω is the frequency of the microwave applied to the resonator. The boundary condition from the coupling of the external transmission line to our single-sided RLR is $a_{\text{in}} + a_{\text{out}} = \sqrt{\kappa_e}a$. Combining these results we finally obtain the reflection coefficient

$$S_{11} = \frac{a_{\text{out}}}{a_{\text{in}}} = -\frac{i(\omega_0 - \omega) + g_{\text{eff}}\chi + \frac{\kappa_i - \kappa_e}{2}}{i(\omega_0 - \omega) + g_{\text{eff}}\chi + \frac{\kappa_i + \kappa_e}{2}}, \quad (11)$$

$$\chi = \frac{g_{\text{eff}}}{i(\Omega - \omega) + \frac{1}{2}\gamma_1 + \gamma_2}. \quad (12)$$

V. FITTING THE FREE PARAMETERS

Figure S4 shows the phase response as a function of probe frequency and the best fit for two typical resonators with $\kappa_e < \kappa_i$ and $\kappa_e > \kappa_i$, respectively. On the basis of these fits, from

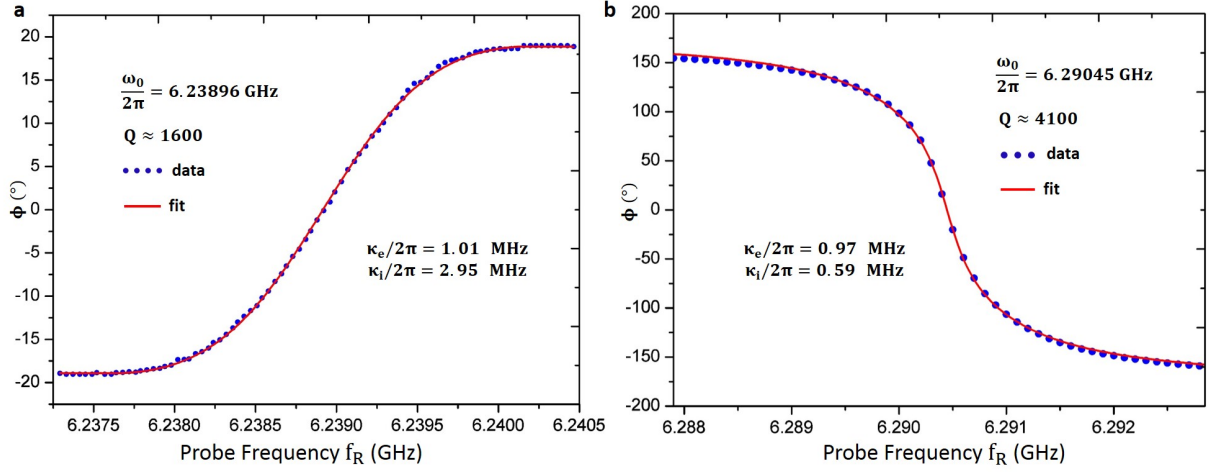


FIG. S4. **Phase response.** The phase response of the resonator as a function of the frequency of the applied microwave signal, together with a fit to the theoretical model. Here we show results for the two cases of $\kappa_e < \kappa_i$ (a) and $\kappa_e > \kappa_i$ (b). The phase response as a function of probe frequency have different shapes depending on whether the internal or external dissipation dominates.

which we obtain the parameters ω_0 , κ_i , and κ_e , we can extract the remaining parameters g_C , $2t_C$, and γ_2 by fitting $\Delta\phi$ as a function of ϵ .

By changing the probe frequency, the shape of phase shift can vary from a single-peak region to a double-peak region (Fig. S5a). The sensitivity of different probe frequencies is shown qualitatively in Fig. S5 b-j, and we conclude that $\Delta\phi$ is more sensitive to γ_2 in the double-peak region than in the single-peak region. Thus, γ_2 can be extracted more accurately by varying the probe frequency such that data from this double-peak region is included in the measurement. Moreover, the double-peak region can be reached by tuning any of the free parameters, including ω , $2t_C$, g_C , γ_1 and γ_2 , as shown in Fig. S6. However, in our experimental setup, $2t_C$ cannot be tuned in-situ like in Refs. [5, 6]. Also, g_C , γ_1 , and γ_2 are fixed for a specific triple point. Compared to tuning $2t_C$, ω is easier to control (accurate to the order of Hz), which can be used to accurately extract of the free parameters $2t_C$, g_C , and γ_2 .

[1] D. Pozar, *Microwave Engineering* (Wiley, 2004).

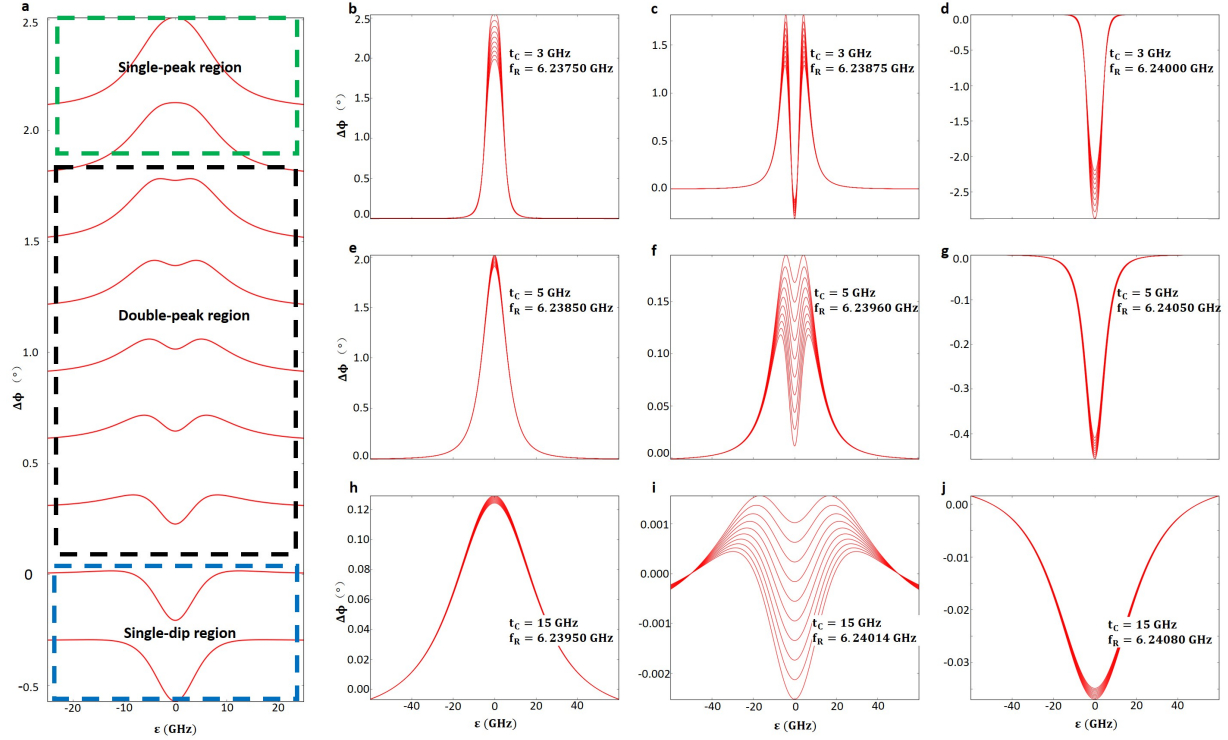


FIG. S5. **Qualitative demonstration of the sensitivity of $\Delta\phi$ on γ_2 for different probe frequencies and t_C** (a) Phase shift as a function of ϵ for different probe frequencies f_R . From the top to the bottom, f_R varies from 6.2393 GHz to 6.2400 GHz, with phase shift curve shape changing from single peak (green box) to double peak (black box) and single dip (blue box). The other parameters are: $t_C = 5$ GHz, $\gamma_2 = 1.65$ GHz, $g_C = 15$ MHz. (b-j) Sensitivity of $\Delta\phi$ on γ_2 in the different regions. The ten curves in each diagram represent γ_2 changing from 1.5 GHz to 2.0 GHz, and $g_C = 15$ MHz is fixed. f_R and t_C are shown in each diagram. In all diagrams (a-j), $\kappa_i = 2.95$ MHz, $\kappa_e = 1.01$ MHz, $\omega_0/2\pi = 6.23896$ GHz, are extracted from the experiment data.

- [2] D. Wei, H.-O. Li, G. Cao, G. Luo, Z.-X. Zheng, T. Tu, M. Xiao, G.-C. Guo, H.-W. Jiang, and G.-P. Guo, arXiv:1307.5663 (2013).
- [3] L. Childress, A. Sørensen, and M. Lukin, Phys. Rev. A **69**, 042302 (2004).
- [4] W. G. van der Wiel, S. De Franceschi, J. M. Elzerman, T. Fujisawa, S. Tarucha, and L. P. Kouwenhoven, Rev. Mod. Phys. **75**, 1 (2002).
- [5] T. Frey, P. J. Leek, M. Beck, A. Blais, T. Ihn, K. Ensslin, and A. Wallraff, Phys. Rev. Lett. **108**, 046807 (2012).

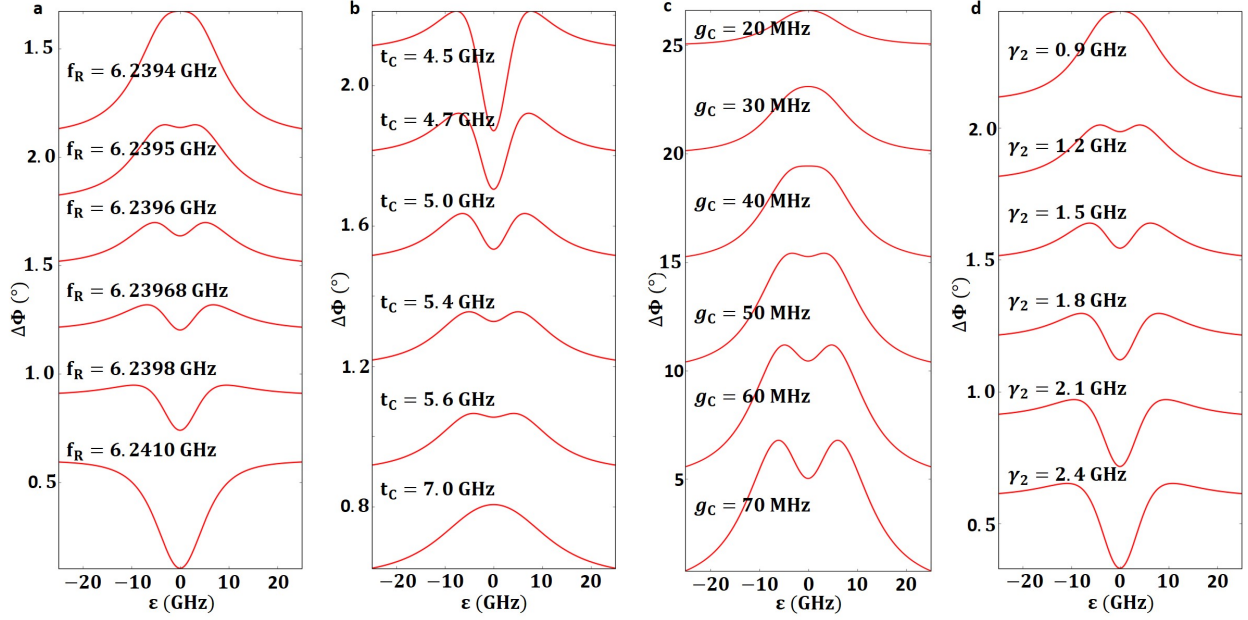


FIG. S6. **Double peak induced by free parameters.** (a) Transition from a region with a single peak, to a double peak, to a single dip, with increasing probe frequency. The other parameters are: $t_C = 5$ GHz, $\gamma_2 = 1.65$ GHz, and $g_C = 15$ MHz. (b) Transition from a double peak to a single peak with increasing interdot coupling strength. Other parameters are: $f_R = 6.23966$ GHz, $\gamma_2 = 1.65$ GHz, $g_C = 15$ MHz. (c) Transition from a single-peak to a double-peak region with increasing resonator-qubit interaction strength. Other parameters: $t_C = 5$ GHz, $f_R = 6.23966$ GHz, $\gamma_2 = 1.65$ GHz. (d) Transition from a single peak, to a double peak, to a single dip with increasing dephasing rate. Other parameters: $t_C = 5$ GHz, $f_R = 6.23966$ GHz, $g_C = 15$ MHz. In all the four panels: $\kappa_i = 2.95$ MHz, $\kappa_e = 1.01$ MHz, and $\omega_0/2\pi = 6.23896$ GHz are extracted from the experiment data.

[6] H. Toida, T. Nakajima, and S. Komiyama, Phys. Rev. Lett. **110**, 066802 (2013).

[7] K. D. Petersson, L. W. McFaul, M. D. Schroer, M. Jung, J. M. Taylor, A. A. Houck, and J. R. Petta, Nature **490**, 380 (2012).